Research in Astronomy and Astrophysics, 22:125016 (12pp), 2022 December https://doi.org/10.1088/1674-4527/ac9c4b

A Possible 250 s X-Ray Quasi-periodicity in the Fast Blue Optical Transient AT2018cow

Wenjie Zhang[1], Xinwen Shu[1], Jin-Hong Chen[2], Luming Sun[1], Rong-Feng Shen[2], Lian Tao[3], Chun Chen[2], Ning Jiang[4], Liming Dou[5], Ying Qin[1], Xue-Guang Zhang[6], Liang Zhang[3], Jinlu Qu[3], and Tinggui Wang[4]
[1] Department of Physics, Anhui Normal University, Wuhu 241002, China; xwshu@ahnu.edu.cn
[2] School of Physics and Astronomy, Sun Yat-Sen University, Zhuhai 519082, China; shenrf3@mail.sysu.edu.cn
[3] Key Laboratory of Particle Astrophysics, Institute of High Energy Physics, Chinese Academy of Science, Beijing 100049, China
[4] CAS Key Laboratory for Researches in Galaxies and Cosmology, Department of Astronomy, University of Science and Technology of China, Hefei 230026, China; twang@ustc.edu.cn
[5] Department of Astronomy, Guangzhou University, Guangzhou 510006, China
[6] School of Physics and Technology, Nanjing Normal University, Nanjing 210023, China
Received 2022 August 25; revised 2022 October 3; accepted 2022 October 5; published 2022 December 7

Abstract

The fast blue optical transients (FBOTs) are a new population of extragalactic transients of unclear physical origin. A variety of mechanisms has been proposed including failed supernova explosion, shock interaction with a dense medium, young magnetar, accretion onto a compact object and stellar tidal disruption event, but none is conclusive. Here we report the discovery of a possible X-ray quasi-periodicity signal with a period of ∼250 s (at a significance level of 99.76%) in the brightest FBOT AT2018cow through the analysis of XMM-Newton/PN data. The signal is independently detected at the same frequency in the average power density spectrum from data taken from the Swift telescope, with observations covering from 6 to 37 days after the optical discovery, though the significance level is lower (94.26%). This suggests that the quasi-periodic oscillation (QPO) frequency may be stable over at least 1.1×10^4 cycles. Assuming the ∼250 s QPO to be a scaled-down analog of that typically seen in stellar mass black holes, a black hole mass of $\sim 10^3$–10^5 solar masses could be inferred. The overall X-ray luminosity evolution could be modeled with a stellar tidal disruption by a black hole of $\sim 10^4$ solar masses, providing a viable mechanism to produce AT2018cow. Our findings suggest that other bright FBOTs may also harbor intermediate-mass black holes.

Key words: black hole physics – X-rays: individual (AT2018cow) – X-rays: bursts

1. Introduction

Recent optical time-domain surveys have discovered a new population of fast-rising blue optical transients (FBOTs). These objects are characterized by rapid rise to their peak brightness within $\lesssim$10 days and blue colors ($g - r < -0.2$) near the peak, followed by fading away of emission within $\lesssim$100 days (Drout et al. 2014; Pursiainen et al. 2018; Ho et al. 2021). AT2018cow is one of the most extreme FBOTs, hosted in the dwarf spiral galaxy CGCG 137-068 at a luminosity distance of 66 Mpc ($z = 0.0141$, Prentice et al. 2018). After its discovery by the ATLAS survey on 2018 June 16, AT2018cow received prompt and extensive multi-wavelength observations spanning from radio to γ-rays (Rivera Sandoval et al. 2018; Ho et al. 2019; Kuin et al. 2019; Margutti et al. 2019; Perley et al. 2019; Roychowdhury et al. 2019; Mohan et al. 2020; Sun et al. 2022; Huang et al. 2019), confirming it to be the brightest FBOT known so far with a peak bolometric luminosity of 4×10^{44} erg s^{-1}, that is located outside the nucleus of the host galaxy with a positional offset of 1.7 kpc. At the explosion site of AT2018cow, a young star population in a dense gas environment was inferred, indicating active star formation (Morokuma-Matsui et al. 2019; Lyman et al. 2020). Despite its physical origin remaining controversial, the multi-wavelength analysis, especially in the X-ray bands, indicates that AT2018cow could be powered by a compact object (Margutti et al. 2019), either a newly formed stellar-mass black hole (BH) or neutron star in a supernova, or tidal disruption of a star by an intermediate-mass black hole (IMBH, a few 10^4–10^5 solar masses) (Kuin et al. 2019; Perley et al. 2019). The detection of 4.4 ms quasi-periodic oscillation (QPO) from NICER observations argues further for the presence of a compact object in AT2018cow (Pasham et al. 2021), but the study is limited to only the soft X-ray band (0.25–2.5 keV) because of the high background contamination beyond ∼2.5 keV. It is still not conclusive whether the compact object is a neutron star or a BH powering AT2018cow.

In this paper, we report the detection of a possible X-ray QPO signal at 4.07 ± 0.39 mHz from XMM-Newton and Swift observations of AT2018cow when its X-ray emission is in the relatively bright phase ($L_{0.3-10\,\mathrm{keV}} \gtrsim 10^{42}$ erg s^{-1}). We also propose a model with the tidal disruption by an IMBH with

mass of $\sim 10^4\,M_\odot$ to explain the unusual X-ray light curve of AT2018cow. In Section 2, we describe the observations and data reduction. Section 3 presents the detailed timing analysis and results. Possible origins of the QPO at ∼4.1 mHz and its implications on the central engine of AT2018cow are discussed in Section 4.

2. Observations and Data Reduction

AT2018cow has been observed by XMM-Newton on three epochs, about 37, 82, and 218 days after the optical discovery. However, only the data from the first XMM-Newton observation have enough photons for detailed timing analysis. We used principally the data from the EPIC PN camera, which have a much higher sensitivity. We processed data using Science Analysis Software version 17.0.0, with the latest calibration files. We extracted the event files from a circular region with a 35″ radius centered on the source position from optical observations (R.A.: $16^{\rm h}16^{\rm m}00\overset{\rm s}{.}22$, decl.: $+22°16'04\overset{''}{.}8$, Prentice et al. 2018) and the background was extracted from four source-free circular regions with 35″ radius near the source position. Both the source spectrum and light curve in the energy range of 0.3–10 keV were selected, and only the good events with PATTERN $\leqslant 4$ were used in generating the light curve. Then we utilized the `epiclccorr` tool to correct the light curve for instrumental effects. By examining the background light curve, we found that background flares were present at the beginning of the observation. We ignored the first ∼3 ks to remove the time interval that may be affected by the high particle background, resulting in a net exposure of ∼27 ks. We assessed the extent of photon pile-up utilizing the SAS task `epatplot`, and found that such an effect is negligible.

AT2018cow was also intensively observed by Swift-XRT covering a period of $t = 3$–70 days since the optical discovery.[7] Totally there are 95 individual Swift-XRT observations in which AT2018cow is detected, which provide critical constraints on the long-term evolution of its X-ray emission. For Swift-XRT data, we executed the task `xrtpipline` to generate the event files, and then used `XSELECT` in HEASoft to extract the source spectrum in a circular region with a radius of 40″, and the background spectrum in an annulus with an inner radius of 60″ and outer radius of 110″. All spectra were extracted in the energy of 0.3–10 keV. The light curves were corrected for bad time intervals using the task `xrtlccorr` and the background was subtracted by applying the standard FTool `lcmath`. Owing to a few counts in individual observations, we cannot derive the source's flux through spectral fittings. We used the `WebPIMMS` tool to convert the Swift-XRT count rates to flux by assuming an absorbed power-law model (Margutti et al. 2019) with photon index $\Gamma = 1.6$ modified by a Galactic HI column density of $N_{\rm H} = 0.05 \times 10^{22}$ cm^{-2}.

[7] We do not use the six Swift-XRT observations at later times ($t = 120$–1380 days), since the source decayed to a flux level not detectable with Swift.

3. Light Curve Analysis and Results

The PN light curve was rebinned to have a time binsize of 10 s. Given the mean count rate of 0.62 cts s^{-1}, this ensures that there are enough photons in each time bin for meaningful timing analysis. We then Fourier transformed the light curve into a power density spectrum (PDS) which was normalized by the Leahy method (Leahy et al. 1983) to have a mean Poisson noise level of 2. The Leahy-normalized PDS was then rebinned by a factor of 21, which gives a frequency resolution of ∼0.8 mHz. Figure 1 (left panel) depicts the resulting PDS, which reveals an apparent QPO component at a frequency of 4.07 ± 0.39 mHz, corresponding to a period of 246 s. We repeated the above analysis by changing the size and position of both source and background extraction areas, and found that the PDS is basically unchanged. In addition, we also checked the PDS of the background light curve and found that there is no QPO signal, so we excluded the possibility that the QPO signal at 4.07 mHz comes from background fluctuations. Furthermore, we checked that the power value ($\xi_{\rm obs} = 4.2$) at the frequency of ∼4.1 mHz does not change if the PDS was constructed from the light curve with smaller time binsizes (<10 s). The QPO signal appears to be present over the entire energy band of our interest (0.3–10 keV), as its power increases gradually if more photons at higher energies are included (Figure A1 in Appendix). However, if focusing on only the hard X-ray bands at >2 keV, the QPO feature disappears, suggesting that the signal is dominated by photons at soft bands.

In order to confirm the QPO detected in the XMM-Newton data, we also performed PDS analysis for data taken from Swift-XRT because its effective energy band is similar to that of XMM-Newton. Due to the individual Swift-XRT observations being short and most having an exposure less than 1 ks, we selected the observations with continuously effective exposure time of >1.25 ks and count rates >0.1 cts s^{-1} to ensure enough counts for timing analysis. This results in a total of 13 useful light curves (Table B1 in Appendix). We further restricted all individual light curve segments to have the same exposure of 1.25 ks for stacking the PDS. The reason to choose the length of 1.25 ks is to ensure that the frequency width of PDS (1/1250 s) is close to that of PN (21/27000 s). Since most of the usable Swift-XRT observations have a length of 1.3–2 ks, we uniformly chose the initial 1.25 ks in each light curve. This will help to avoid the effect of arbitrarily selected light curve segments that may cause false signals in the PDS. Note that we split one light curve that has enough exposure length (2.8 ks) into two 1.25 ks segments. The light curve segments were rebinned to have a time binsize of 10 s, resulting in at least 1 count per bin,

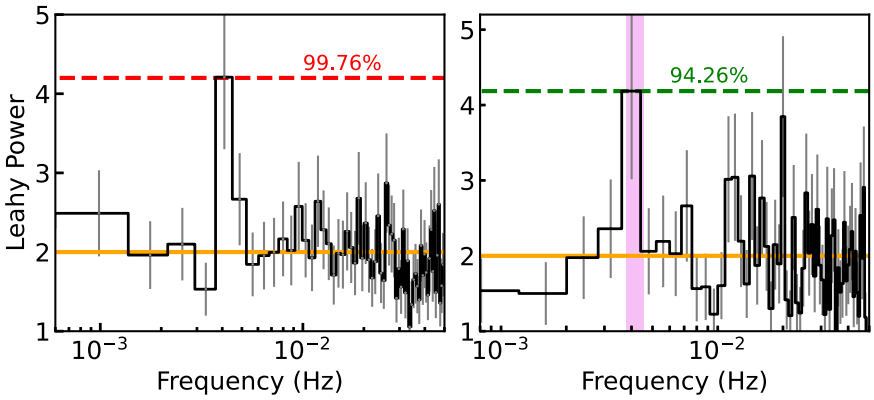

Figure 1. XMM-Newton and Swift PDS for AT2018cow. (Left) XMM-Newton Leahy-normalized PDS of AT2018cow in 0.3–10 keV. The PDS was binned to have a frequency resolution of 0.78 mHz. A strong peak appears at 4.07 ± 0.39 mHz (≈246 s), indicating the presence of a QPO component. The QPO frequency is defined as the centroid value of the peak frequency bin, and the error is half of the bin width. The red dashed line corresponds to the 99.76% confidence level derived from Monte Carlo simulations. The orange horizontal line indicates the white noise (the value is 2 in Leahy-normalized power spectrum). (Right) Averaged Swift PDS with a frequency resolution of 0.8 mHz. The green dashed line represents the 94.26% confidence level. The purple strip signifies the location of QPO in XMM-Newton. The error bars mean 1σ uncertainties.

which is sufficient for a reliable timing analysis. By stacking the PDS from totally 13 individual light curve segments, each with 1.25 ks, we extracted an average PDS for the Swift-XRT data. The Leahy-normalized PDS is displayed in Figure 1 (right panel) where an obvious feature is observed at 4.0 ± 0.4 mHz, which is consistent with the QPO frequency obtained with the XMM-Newton data within errors. Note that the Leahy-normalized PDS was produced without weighting by flux for the Swift-XRT data, as it is not clear whether there is a strong dependence of QPO strength on the X-ray flux.

We also used the light curve analysis tool `efold` in HEASoft to fold the PN light curve with the period of 246 s, which is shown in Figure 2. The fractional root mean square (rms) amplitude calculated by the folded light curve is $6.0\% \pm 1.3\%$. The light curves from individual Swift observations do not have enough signal-to-noise ratio values to perform the folded analysis. Therefore, we did not estimate the QPO rms amplitude for the Swift data.

To estimate the statistical significance of the QPO detected at ∼4.1 mHz which depends on the underlying distribution of the noise powers, an important question is to test whether the noise at other frequencies (except for the frequency where the QPO is located) in the PDS is consistent with white noise which is relatively flat, or red noise whose strength depends on frequency. A direct way to distinguish the type of noise is to examine whether the noise powers are χ^2 distributed as expected for white noise. We removed the three frequency bins centered at 4.1 mHz, and generated a cumulative distribution function (CDF) of the powers at all other frequencies. We then compared it with a χ^2 distribution (with 2×21 degrees of freedom, d.o.f.) scaled by a factor of $1/21$, where the number 21 is the factor by which the PDS was

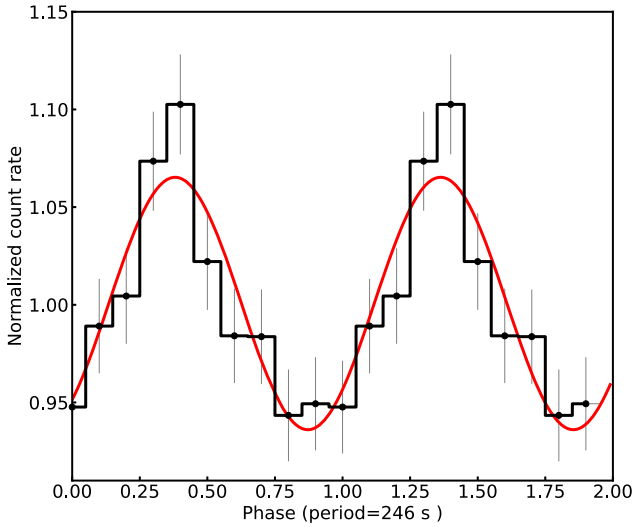

Figure 2. XMM-Newton folded light curve in 0.3–10 keV with a period of 246 s, and the best-fit sinusoid is drawn as a red solid line. The error bars represent 1σ uncertainties.

rebinned, as displayed in Figure C1 in the Appendix. In addition, we also analyzed the probability density distribution of these powers and compared it with the expected values from a χ^2 distribution. Both tests yield consistent results that the powers of the noise can be described with a χ^2 distribution, i.e., dominated by white noise. For the Swift PDS, we also tested that the noise powers are χ^2 distributed (Figure C1 in the Appendix). Therefore, for the white noise distribution of the underlying continuum in the PDS, the significance of the QPO at ∼4.1 mHz can be analytically estimated using the χ^2 distribution. For the XMM-Newton data, we found that the probability to observe a power value larger than measured

($\xi_{\rm obs} = 4.2$) is $P\,(>21\xi_{\rm obs}; {\rm d.o.f.}) = 3.9 \times 10^{-5} = p_1$. By taking into account the search for all frequency bins over the range of interest ($N = 64$), the global significance is $1 - p_1 \times N = 99.75\%$. Similarly, for the Swift PDS, the probability to observe a power value larger than measured ($\xi_{\rm obs} = 4.18$) is $P\,(>13\xi_{\rm obs}; {\rm d.o.f.}) = 9.26 \times 10^{-4} = p_2$. The global confidence level for $N = 62$ frequency trials is $1 - p_2 \times N = 94.26\%$.

The above assessment of noise distribution in the PDS is only qualitative. It is still possible that a weak or unknown red noise component is present in the data. To estimate the QPO significance by properly accounting for the underlying noise, we then employed a Monte Carlo approach, by generating a series of light curves following a given power spectral distribution (Uttley et al. 2002). We used the power-law plus constant model, $P(f) = Nf^{-\alpha} + C$, to fit the unnormalized and unbinned PDS of XMM-Newton, where N is the normalization factor, α is the power-law index and C is a constant indicating the Poisson noise level. The power-law component was used to account for a possible effect of weak red noise on the simulation results. Using the maximum likelihood estimation method (Vaughan 2010), we first obtained the best fitting parameters, where $N = -0.71$, $\alpha = -1.1 \times 10^{-5}$ and $C = 5.04$. Then we utilized the best-fit PDS model to generate a series of simulated light curves (Timmer & Koenig 1995), which were resampled to have the same duration, mean count rate and variance as the real light curve. To eliminate the possible effect of red noise leakage at the edge of the light curve, we chose a length of $5 \times 27{,}000$ s which is five times longer than the real data. Then we intercepted the middle 27 ks as the final light curve for simulations. We repeated this process and obtained 100,000 simulated light curves. The same power spectral analysis on these simulated light curves was performed as we did on the real data, producing 100,000 simulated PDS.

With the 100,000 simulated PDS, we computed the significance level of a QPO peak by scanning all frequency bins below 0.05 Hz, the highest frequency in the PDS. We averaged the power of the 100,000 PDSs at each frequency bin and obtained the $\langle P_{f_i} \rangle$ where i is ith number of bins ($i = 1,...,n$). For each simulated PDS, we divided the power value at each frequency by the average value $\langle P_{f_i} \rangle$ at the corresponding frequency, and recorded the largest value as $\xi_{\rm max}$, yielding 100,000 $\xi_{\rm max}$ at a given frequency. Averaging the power distribution has the advantage of eliminating the possible effect of red noise (Pasham et al. 2019). Using the 100,000 values of $\xi_{\rm max}$, we calculated the cumulative distribution of probability to exceed a given $\xi_{\rm max}$ (Figure 3). By comparing with the observed value of $\xi_{\rm max,obs}$, we obtained the global confidence level of 99.76% for the QPO at ~4.1 mHz. Using the same Monte Carlo approach, we obtained that the statistical significance of the QPO signal in the Swift PDS is 94.38%. The results from Monte Carlo simulations are in good agreement with those obtained with the χ^2 analysis of white noise distribution, indicating that the red noise component (if present) is negligible. Considering that the QPO was detected at the same frequency in two independent detectors, its combined confidence level is 99.986%, making the signal statistically significant. Note that we did not detect the QPO signal in either individual or combined EPIC MOS data, possibly due to the relatively low count rates in the individual MOS light curves, which are a factor of ~3.5 less than those in PN. In addition, the fractional rms amplitude is only 6%, implying that the QPO signal (if present) could be more affected by noise fluctuations in the MOS data. In order to test this possibility, we performed detailed simulations in Appendix D, and found that the chance of the same QPO signal detected at a level of 99.76% in the MOS data is indeed low (<0.1%). We also performed the PDS analysis by combining PN and MOS light curves, and found that the power value at 4.1 mHz comes down, probably due to the fact that QPO signal is not detectable in the MOS data. In this case, the global confidence level for the QPO in the combined light curve is reduced to 92.81% (Figure D2).

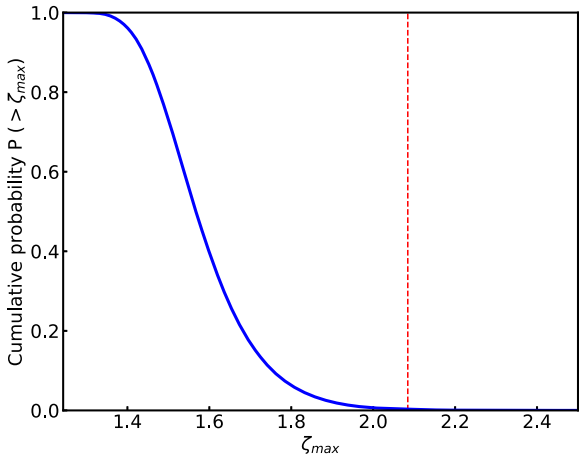

Figure 3. Cumulative distribution of the maximum noise power $P(>\xi_{\rm max})$ from Monte Carlo simulations. The red dashed line marks $\xi_{\rm max,obs}$ measured from the XMM-Newton data. By comparing $\xi_{\rm max,obs}$ with the cumulative distribution of noise power, we derived a global statistical significance of 99.76% for the QPO detected in the XMM-Newton data. All the power values were divided by the average value at the corresponding frequency bin (Section 3 for details).

4. Discussion and Conclusions

Having established that the QPO is statistically significant, we now place its constraint on the origin of the X-ray emission and the central engine of AT2018cow. On the basis of the soft X-ray QPO identified at 224 Hz, a compact object for the origin of X-ray emission was proposed (Pasham et al. 2021). The discovery of ~4.1 mHz QPO provides further evidence for the presence of a compact object, which could be either a neutron

star or an accreting BH. mHz QPOs have been detected in a few neutron-star low-mass X-ray binaries (Revnivtsev et al. 2001; Tse et al. 2021), which are generally explained as thermonuclear burning on the neutron star surface. As a result, these QPOs are transient behavior occurring only in a narrow range of X-ray luminosity during outbursts. This contradicts the constant frequency of the QPO at ∼4.1 mHz in AT2018cow, as the stacking analysis of Swift data suggests that the QPO frequency may be stable over a period of 30 days, during which the luminosity declined by a factor of >5. The QPO's stability may also challenge other models involving a neutron star (Pasham et al. 2021), such as spin-down of an isolated millisecond magnetar or magnetar-accretion driven outburst.

If the compact object was a stellar-mass BH, the 4.1 mHz QPO is unlike typical low-frequency QPOs (LFQPOs), as the frequency is lower than most of the type-A (∼8 Hz), type-B (∼5–6 Hz) and type-C (∼0.1–15 Hz) QPOs (Casella et al. 2005; Remillard & McClintock 2006; Ingram & Motta 2019). The QPO's frequency is also far less than a few 10–100 Hz for high-frequency QPOs (HFQPOs) (Morgan et al. 1997; Belloni et al. 2012). Although several accreting stellar-mass BHs have exhibited QPOs with frequency in the mHz range (Cheng et al. 2019), most of these sources are believed to have high orbital inclinations. This is inconsistent with the weak or no X-ray absorption in observations on timescales of hours to days (Margutti et al. 2019). Furthermore, almost all these sources have shown the red noise PDS at below 1 mHz. These properties distinguish them from the 4.1 mHz QPO found in AT2018cow, which appears with weak or absent red noise. Two BH sources, GRS 1915+105 and IGRJ17091–3624, show mHz QPOs in the so-called "heartbeat" state (Belloni et al. 2000; Altamirano et al. 2011). However, these QPOs are characterized by high harmonic content and accompanied with flat-top noise in the PDS where low and high frequency breaks are evident. On the other hand, if isotropically emitted, the peak luminosity of AT2018cow is $\gtrsim 10^4$ times the Eddington limit for a stellar-mass BH ($M_{\rm BH} \sim 10\,M_\odot$), challenging standard models of BH accretion. Therefore, if the mHz QPO of AT2018cow was due to a process similar to that operating in stellar-mass BHs, the underlying physical mechanism would be extreme and have never been seen before.

The observed frequency, if it is related to the Keplerian period of the innermost circular stable orbit, would correspond to a BH mass of between $5 \times 10^5\,M_\odot$ and $6 \times 10^6\,M_\odot$, for a non-rotating and maximally rotating BH, respectively. Alternatively, the 4.1 mHz QPO could represent a scaled-down analog of the typical LFQPOs or HFQPOs of stellar-mass BHs, but occurring at a lower frequency if a more massive BH or IMBH is at work in AT2018cow. The frequencies of HFQPOs appear to be stable and scale inversely with mass, $f_0 = 931\,(M/M_\odot)^{-1}$ Hz (Remillard & McClintock 2006). Assuming the 4.1 mHz corresponds to the stronger $2 \times f_0$ frequency, the scaling relation yields a BH mass of $4.4 \times 10^5\,M_\odot$ in AT2018cow (Figure 4). As we mentioned above, different types of LFQPOs are observed in the frequency range of ∼0.1–20 Hz. The QPO frequency can be variable and correlated with the energy spectral parameters, i.e., the flux and shape of a power-law spectral component (Remillard & McClintock 2006). During the first 37 days, the 0.3–10 keV spectrum of AT2018cow can be described by a simple power-law with little absorption (Margutti et al. 2019), with a photon index in the range ∼1.6–1.7, indicating no evident spectral evolution. Following the method outlined in previous works (Dewangan et al. 2006; Strohmayer & Mushotzky 2009), we used the relation between the QPO frequency and power-law index obtained for six systems with dynamic mass constraints (Vignarca et al. 2003; Shaposhnikov & Titarchuk 2009; Strohmayer & Mushotzky 2009) to find the possible range of QPO frequencies with power-law indices between 1.6 and 1.7. Under the assumption that QPO frequency scales inversely in proportion to BH mass (Remillard & McClintock 2006), we can estimate the BH mass in AT2018cow to be $M_{\rm BH} \sim 2.2 \times 10^3\,M_\odot$ (Figure 4). The above estimates of the BH mass ($\sim 10^3$–$10^5\,M_\odot$) suggest that AT2018cow may harbor an IMBH.

In order to explain its fast evolving ultraviolet (UV) and optical emission, Perley et al. (2019) suggested that AT2018cow could be powered by the TDE of a main sequence star by an IMBH. They used the MOSFit TDE model (Mockler et al. 2019) to fit the UV and optical light curves and obtained a best-fit BH mass of $1.9 \times 10^4\,M_\odot$ disrupting a star of 0.6 $M_\odot$. However, it is possible that the early UV and optical emission originates from the circularization process (Piran et al. 2015), rather than accretion, posing a challenge to apply the MOSFit model which assumes the TDE UV/optical emission is related to the reprocessed accretion luminosity. We attempted to develop a TDE accreting model to fit its X-ray light curve obtained from Swift-XRT observations. In this framework, after a star is disrupted by the BH, its debris will fall back to the pericenter on a timescale (Rees 1988)

$$t_{\rm fb} \simeq 4.1 \left(\frac{M_{\rm BH}}{10^4\ M_\odot}\right)^{1/2} \times \left(\frac{M_*}{M_\odot}\right)^{-1} \left(\frac{R_*}{R_\odot}\right)^{3/2} \text{days}, \quad (1)$$

where $M_{\rm BH}$ is the BH mass, M_* is the mass of the disrupted star and R_* is its radius. In the late time, the fallback rate $\dot{M}_{\rm fb}(t)$ drops with an asymptotic power-law index $-5/3$ (Ramirez-Ruiz & Rosswog 2009; Chen & Shen 2018). However, the power-law index can approach $-9/4$ rather than the canonical value of $-5/3$, if the stellar core survives after the pericentric

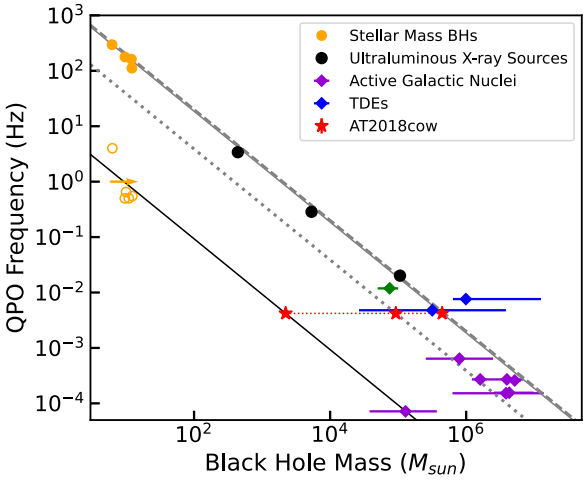

Figure 4. Relation between QPO frequency and BH mass. The gray solid line is the extrapolation of the relation between QPO frequency and BH mass for stellar mass BHs derived in Remillard & McClintock (2006), assuming that the QPO corresponds to $2 \times f_0$ for the 3:2 harmonic peaks. The dashed and dotted lines represent the relation derived from the model of 3:2 resonance (Aschenbach 2004) with the spin parameters $a = 0$ and $a = 0.998$, respectively. The HFQPOs are shown in filled orange circles (Strohmayer & Mushotzky 2009; Zhou et al. 2015), while LFQPOs are represented with open orange circles. The frequencies of LFQPOs are derived using the relation between frequency and spectral index (Shaposhnikov & Titarchuk 2009), with the 0.3–10 keV spectral index ranging from 1.6 to 1.7 as observed in AT2018cow. Only the stellar-mass BHs with dynamic mass constraints are displayed. The data for ultraluminous X-ray sources harboring IMBHs, tidal disruption events (TDEs) (ASASSN-14li and Sw J1644+57) and active galactic nuclei (AGNs) with supermassive BHs are taken from Reis et al. (2012); Pasham et al. (2015, 2019); Song et al. (2020). The gray solid line is scaled downward by a factor of 200 to approximately match the distribution of LFQPOs. The AT2018cow's BH mass range constrained by the 4.1 mHz QPO is shown by red stars. The errors on BH mass are reported to take into account the statistical errors and typical errors of ∼0.5 dex for the scaling relation between the BH mass and host properties.

encounter (Guillochon & Ramirez-Ruiz 2013; Coughlin & Nixon 2019) or the disrupted star is in its late age (Golightly et al. 2019). The luminosity history will trace the mass fallback rate if the fallback mass is rapidly accreted by the BH. In this case, accretion rate $\dot{M}_{\rm acc}$ will be close to the fallback rate $\dot{M}_{\rm fb}$, and the luminosity is $L(t) = \eta \dot{M}_{\rm fb} c^2$, where $\eta \ll 1$ is the efficiency of converting accretion power to luminosity. However, this might not be occurring if the accretion timescale is longer than the fallback timescale. In this case, the relation between the accretion rate and the mass fallback rate can be given by Kumar et al. (2008); Lin et al. (2017); Chen & Shen (2018); Mockler et al. (2019)

$$\dot{M}_{\rm acc}(t) = \frac{1}{\tau_{\rm acc}} \times \left(e^{-t/\tau_{\rm acc}} \int_{t_{\rm fb}}^{t} e^{t'/\tau_{\rm acc}} \dot{M}_{\rm fb}(t')\, dt' \right), \quad (2)$$

where $\tau_{\rm acc}$ is the so-called "slowed" accretion timescale.

Here we approximate the overall debris fallback history as follows. The fallback rate remains constant at $\dot{M}_{\rm peak}$ between $t_{\rm fb}$ and $1.5t_{\rm fb}$, and after $1.5t_{\rm fb}$ it starts to decay as $t^{-5/3}$, i.e.,

$$\dot{M}_{\rm fb} = \begin{cases} 0, & t \lesssim t_{\rm fb} \\ \dot{M}_{\rm peak}, & t_{\rm fb} \lesssim t \lesssim 1.5t_{\rm fb} \\ \dot{M}_{\rm peak} \left(\dfrac{t}{1.5t_{\rm fb}} \right)^{-5/3}, & t \gtrsim 1.5t_{\rm fb}. \end{cases} \quad (3)$$

For the case of full disruption, $\dot{M}_{\rm peak} \simeq 0.2 M_{*}/t_{\rm fb}$. The luminosity history is $L(t) = \eta \dot{M}_{\rm acc} c^2$. If the "slowed" accretion timescale is $\tau_{\rm acc} = 0$, it becomes $L(t) = \eta \dot{M}_{\rm fb}(t) c^2$. We used the parameter η, BH mass $M_{\rm BH}$ and TDE start time t_0 to fit the X-ray light curve. The disrupted star is assumed to be solar-type. The best fitting result yields $M_{\rm BH} \sim 10^4\, M_{\odot}$, $t_0 \sim 58{,}281$ (Modified Julian Date days), $\tau_{\rm acc} \sim 9$ days and $\eta \sim 10^{-5}$. The corresponding fallback timescale is $t_{\rm fb} \sim 4$ days. The best-fit light curve is depicted in Figure 5 for the late-time luminosity evolution parameterized with $t^{-5/3}$ decline law (black), and with $t^{-9/4}$ decline law (red).

The best-fit TDE model yields a BH mass of $\sim 10^4\, M_{\odot}$, which is consistent with the mass range constrained by the QPO analogy, as well as that obtained by fitting the MOSFit model to the UV/optical emission of AT2018cow (Mockler et al. 2019). Given the observed peak bolometric luminosity of $\sim 4 \times 10^{44}$ erg s^{-1} (Margutti et al. 2019), such a BH mass requires that the system be radiating at about 100 times the Eddington limit. On the other hand, the X-ray emission may be anisotropic and beamed, given the detections of fast-evolving radio radiation (Margutti et al. 2019; Bietenholz et al. 2020; Mohan et al. 2020). The X-ray timing and spectral properties, i.e., QPO frequency, rms amplitude and power-law dominated X-ray spectrum, make AT2018cow similar to the jetted TDE Sw J1644+57 (Reis et al. 2012), though the latter has a much higher luminosity, indicating that similar processes may operate in two objects.

We note that Pasham et al. (2021) identified a soft X-ray QPO at a much higher frequency of 224 Hz, setting a tight mass limit for the compact object in AT2018cow to be less than 850 $M_{\odot}$ if due to a BH. If the signal were true, the tension could be alleviated by introducing a binary compact object system instead of a single neutron star or BH. Such an exotic system comprised of a stellar-mass compact object orbiting around an IMBH with mass $\sim 10^3$–$10^5\, M_{\odot}$, if confirmed, would be a valuable gravitational wave source for future space-based missions such as the Laser Interferometer Space Antenna (Babak et al. 2017). In conclusion, our results suggest that the FBOT AT2018cow may be powered by an IMBH residing in young star clusters off-center from its dwarf host galaxy (Morokuma-Matsui et al. 2019). Although a variety of searching strategies has been proposed (Noyola et al. 2008; Farrell et al. 2009; Lin et al. 2018; Greene et al. 2020), the existence of IMBHs is still in

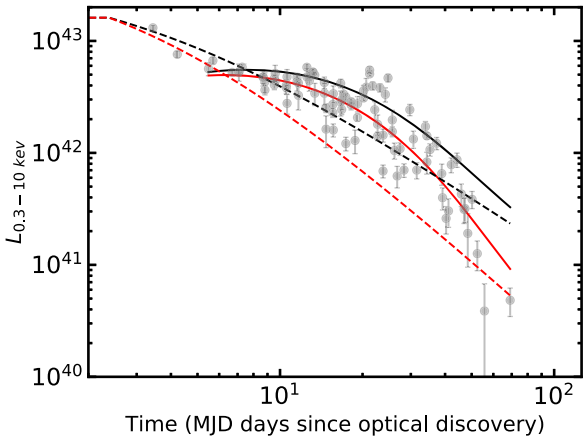

Figure 5. The best-fit result to the X-ray light curve applying the TDE model. The X-ray luminosity was derived using the data from Swift-XRT observations (Section 2). The solid lines represent the best-fitting light curve for the viscously slowed accretion model. The dashed lines correspond to the light curve with $\tau_{\rm acc} = 0$. The black and red lines are for the luminosity evolution models assuming a power-law index of $L \propto t^{-5/3}$ and $L \propto t^{-9/4}$ at later times, respectively. The latter steeper power-law index is predicted if the stellar core survives after the pericentric encounter (Guillochon & Ramirez-Ruiz 2013; Coughlin & Nixon 2019) or the disrupted star is in its late age (Golightly et al. 2019). The best-fitting gives the "slowed" accretion timescale $\tau_{\rm acc} \sim 9$ days, the black mass $M_{\rm BH} \sim 10^4\,M_{\odot}$ and the corresponding fallback timescale is $t_{\rm fb} \simeq 4$ days if the disrupted star is solar-type.

dispute. Luminous FBOTs are promising candidates in future search for IMBHs, which will provide further insights into their formation mechanisms.

Acknowledgments

This research made use of the HEASARC online data archive services, supported by NASA/GSFC. We thank the P.I. who proposed the XMM-Newton and Swift observations of AT2018cow for making the data available. This work is supported by the National Natural Science Foundation of China (NSFC, Grant Nos. 11822301, 12192220, 12192221 and 11833007). X.S. acknowledges support by the science research grants from the China Manned Space Project through No. CMS-CSST-2021-A06. L.T. acknowledges support from the NSFC (Grant No. 12122306). J.Q. acknowledges support from the NSFC (Grant Nos. 11733009 and U2031205).

Appendix A
Comparison of XMM-Newton PDS at Different Energy Bands

Figure A1 shows the XMM/PN PDS extracted in different energy bands.

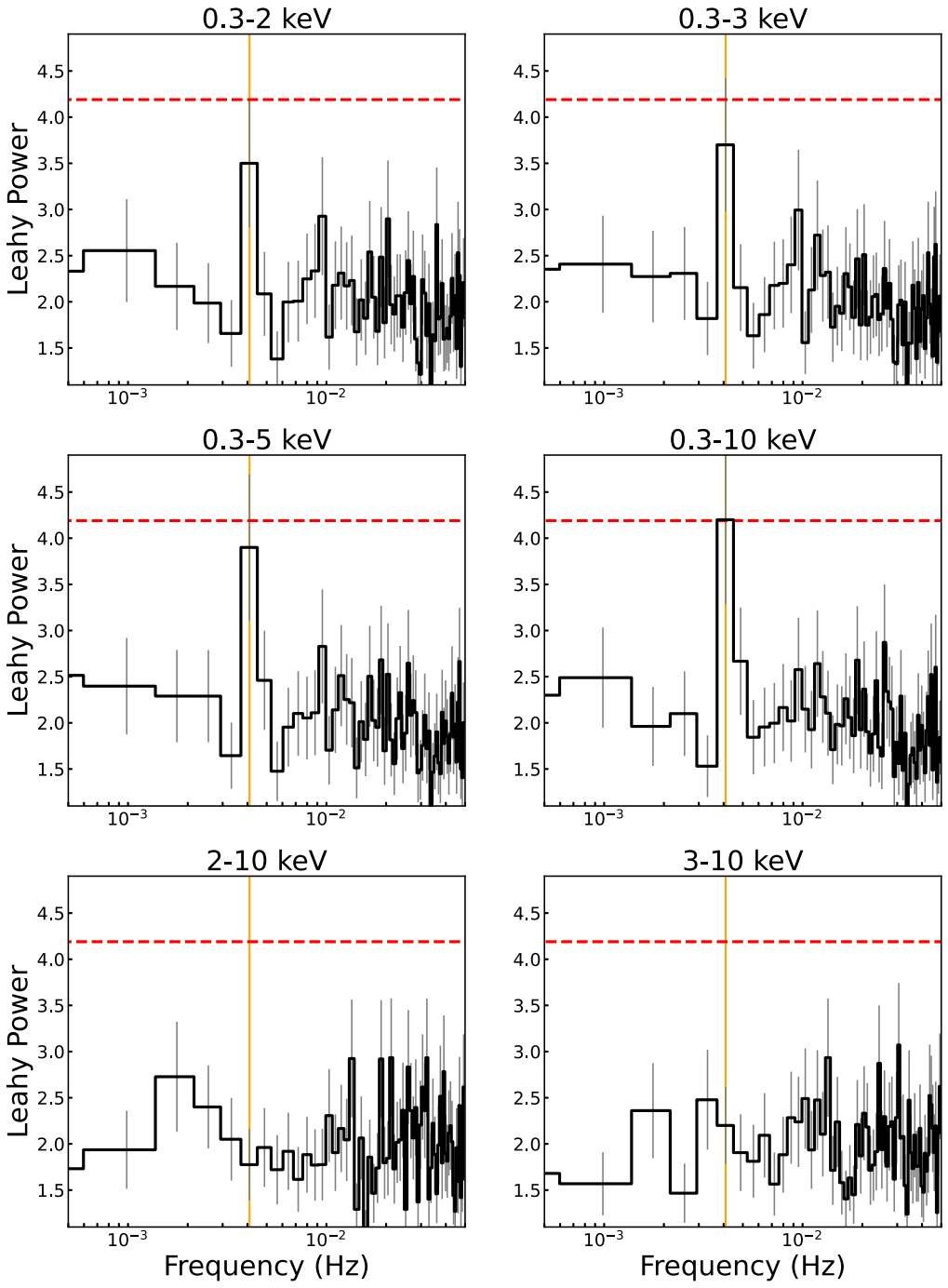

Figure A1. The PDS of XMM-Newton/PN light curve constructed at six different energy bands. The red dashed line represents the power value corresponding to the 99.76% confidence level, while the orange line shows the QPO frequency at 4.1 mHz.

Appendix B
Swift-XRT Data Used in the PDS Analysis

Table B1 lists Swift data used in the PDS analysis (Section 3). For the observation of S11, the light curve can be divided into two segments with 1.25 ks. All other $\geqslant$2.5 ks observations cannot be divided into two segments due to the presence of a gap in the light curve. Note that we extracted the average PDS from the light curve segments for the NuSTAR and NICER observations, but did not detect the QPO signal at 4.1 mHz. This is possibly due to the fact that the QPO signal is dominated by photons at soft bands (Figure A1), while only data in the hard X-ray band at $>$3 keV can be used for NuSTAR observations. For NICER observations, most light curve segments have too short exposures ($\lesssim$1 ks) to be used effectively in searching for the QPO signal through stacking PDSs. Hence, we do not display the NuSTAR and NICER data in this paper.

Table B1
Swift-XRT Data Used in the PDS Analysis

No.	ObsID	Exposure (ks)	Obs. Date	Days	Segment
S1	00010724009	1.3	2018-06-22	6	1
S2	00010724010	1.4	2018-06-23	7	1
S3	00010724019	1.3	2018-06-25	9	1
S4	00010724037	1.4	2018-06-29	13	1
S5	00010724041	1.3	2018-06-30	14	1
S6	00010724043	1.3	2018-07-01	15	1
S7	00010724051	1.2	2018-07-03	17	1
S8	00010724054	2.1	2018-07-04	18	1
S9	00010724057	2.7	2018-07-05	19	1
S10	00010724060	2.5	2018-07-06	20	1
S11	00010724063	2.8	2018-07-07	21	2
S12	00010724067	2.5	2018-07-08	22	1

Appendix C
Tests for Noise Properties in the PDS of XMM-Newton and Swift Data

Figure C1 (upper row) shows the CDF (left) and probability density function (right) of noise powers in the PDS of XMM-Newton data.

It is evident that the observed noise powers are consistent with a χ^2 distribution (with 2×21 d.o.f., see Section 3 for details) scaled by a factor of $1/21$, i.e., consistent with white noise. Note that we performed similar analysis of noise properties in the PDS of Swift/XRT data, and found the noise power values are also χ^2 distributed (lower row).

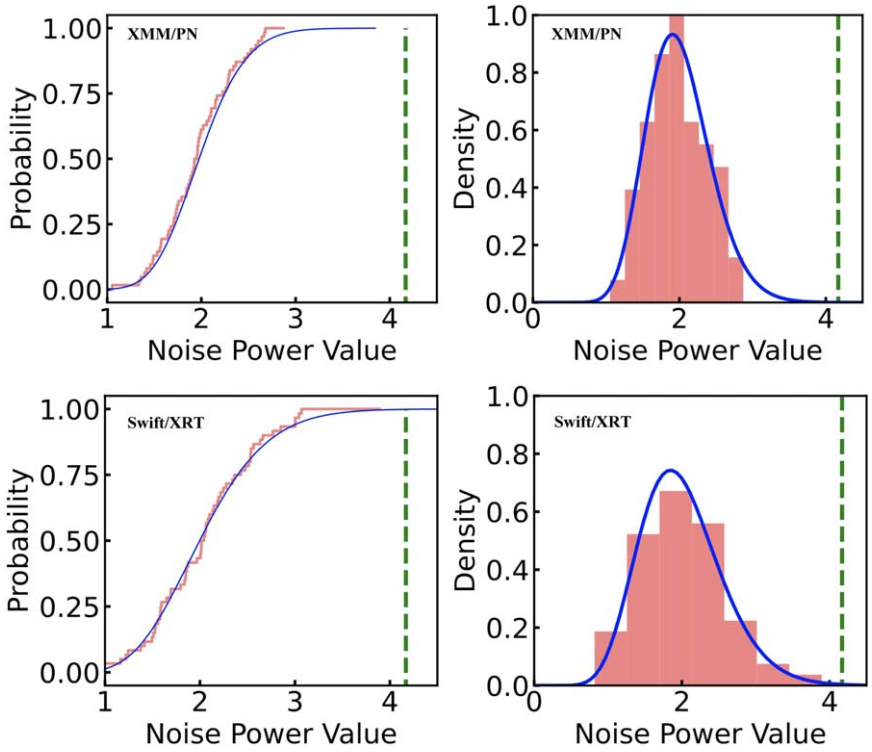

Figure C1. Tests for noise properties in the PDS of XMM-Newton (upper row) and Swift (lower row) data. Left: the red step line shows the CDF of noise power below 0.05 Hz. The three frequency bins centered at 4.1 mHz were removed. The blue curve represents the expected χ^2 distribution. It can be seen that the blue curve is in good agreement with the CDF of the observational data. Right: the red histogram displays the density distribution of noise powers, which is consistent with the expected χ^2 distribution for white noise (blue curve). The green dashed line indicates the power value at 4.1 mHz for XMM/PN and Swift/XRT.

Appendix D
Tests on the Detectability of the 4.1 mHz QPO in the XMM-Newton/MOS Data

We reduced the data from XMM-Newton/MOS observations (MOS1 and MOS2) following the standard procedures utilizing the XMM-Newton SAS v17.0.0, with the latest calibration files. Similar to PN, the source light curves in the energy range of 0.3–10 keV were extracted using a circular region with a radius of 35″, while the background light curves were extracted from source-free areas on the same CCD using four identical circular regions. No strong background flares were present during the MOS observations. Figure D1 (upper panel) displays the MOS1, MOS2 and MOS1+MOS2 light curves. Then we produced the corresponding Leahy-normalized PDS with a frequency resolution of 0.8 mHz (Figure D1, lower panel), where no strong feature at 4.1 mHz can be seen, with the power values being consistent with the noise level of ∼2. This suggests that even if we combine the PN and MOS data, the signal would not necessarily be getting stronger (Figure D2).

Furthermore, we performed simulations to assess whether the 4.1 mHz QPO signal of AT2018cow seen in the PN data (at 99.76%) is indeed not detectable by MOS. We generated a fake MOS1 light curve as follows. We first divided the observed source light curve of PN by a factor of 3.5 (the ratio of mean count rates between PN and MOS1), and added the observed background light curve of MOS1 to resemble the expected source+background light curve of MOS1. By assuming a Poisson distribution, we then re-sampled the expected counts in each time bin. Finally, we subtracted the observed background counts from the expected counts to produce a fake source light curve of MOS1. We also generated a fake MOS2 light curve in a similar way. We repeated the procedures 10^4 times and obtained 10^4 simulated MOS1+MOS2 light curves and PDSs.

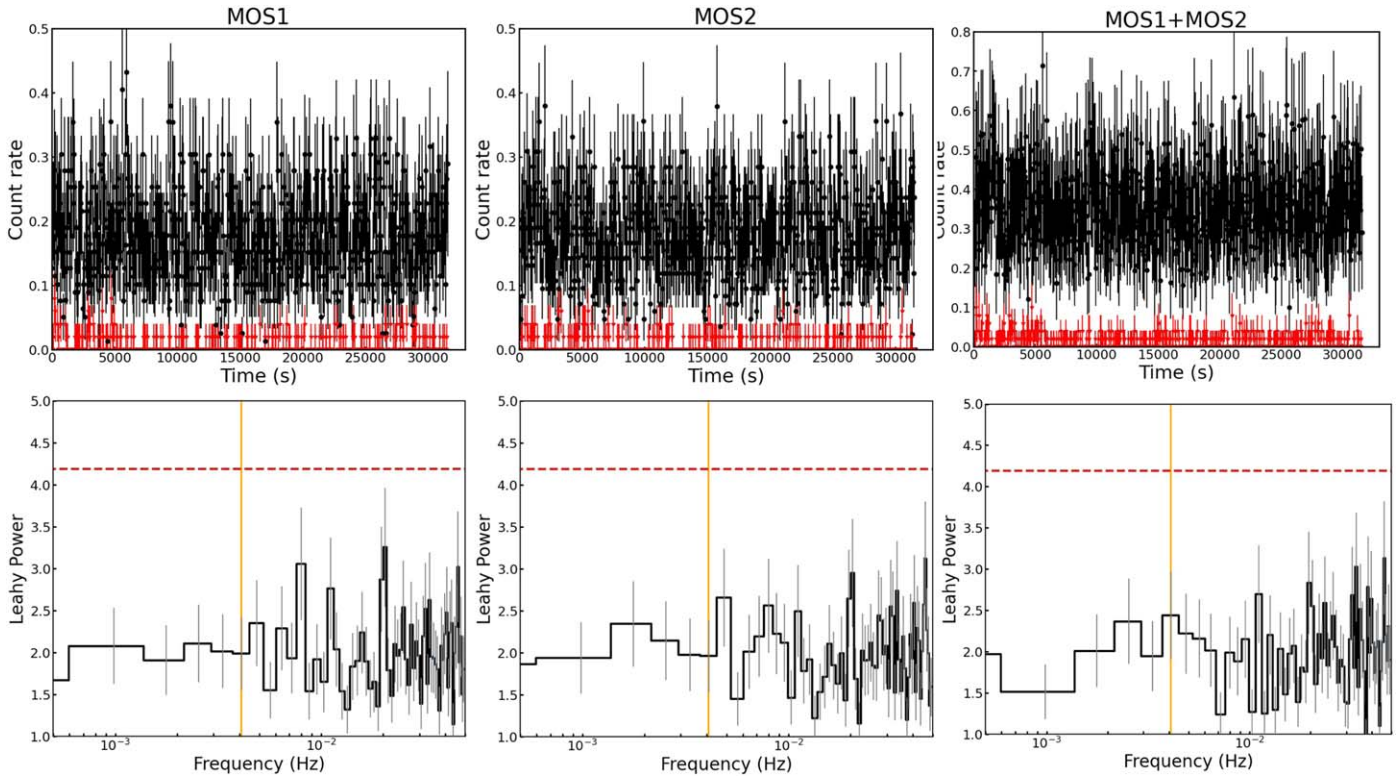

Figure D1. XMM-Newton MOS1, MOS2 and MOS1+MOS2 light curves (upper panel), and the corresponding PSD (lower panel). The background light curves are shown in red. The red dashed line represents the 99.76% confidence level for the QPO detected at the frequency of 4.1 mHz in the PN data (orange vertical line, see Figure 1 for details).

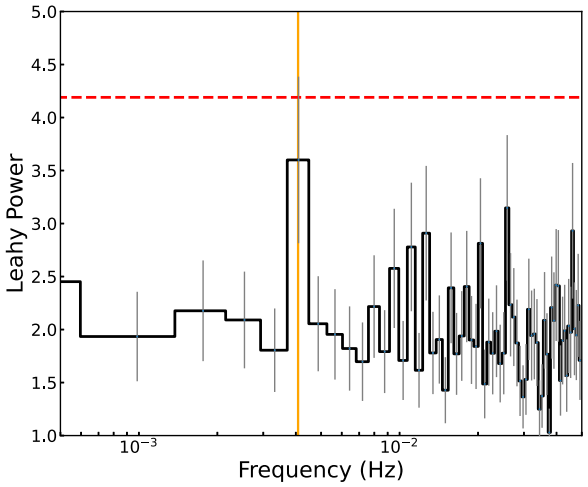

Figure D2. The Leahy-normalized PDS constructed by combining PN and MOS light curves.

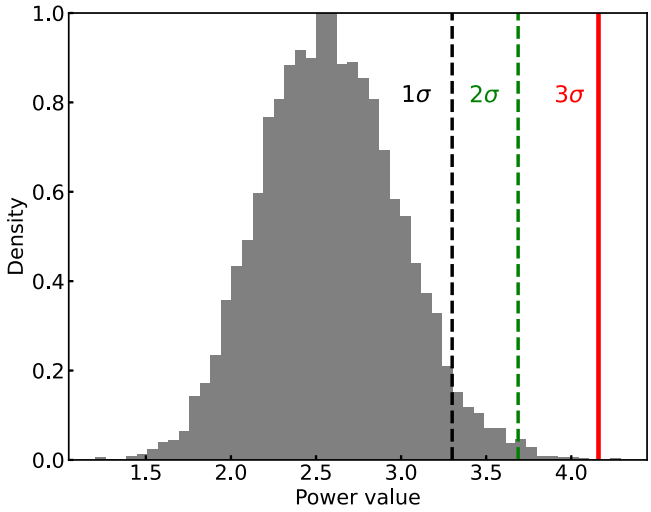

Figure D3. Distribution of power values at 4.1 mHz from light curve simulations by decreasing the PN count rates to mimic the MOS (MOS1 +MOS2) ones. The vertical lines represent the 1, 2 and 3σ confidence levels obtained from the simulated MOS PDS.

Among 10^4 PDS, only seven have power values at 4.1 mHz reaching the 99.76% level as detected in PN (Figure D3). This suggests that the chance of QPO detection in the MOS data is indeed low (<0.1%).

References

Altamirano, D., Belloni, T., Linares, M., et al. 2011, ApJL, 742, L17
Aschenbach, B. 2004, A&A, 425, 1075
Babak, S., Gair, J., Sesana, A., et al. 2017, PhRvD, 95, 103012
Belloni, T., Klein-Wolt, M., Méndez, M., van der Klis, M., & van Paradijs, J. 2000, A&A, 355, 271
Belloni, T. M., Sanna, A., & Méndez, M. 2012, MNRAS, 426, 1701
Bietenholz, M. F., Margutti, R., Coppejans, D., et al. 2020, MNRAS, 491, 4735
Casella, P., Belloni, T., & Stella, L. 2005, ApJ, 629, 403
Chen, J.-H., & Shen, R.-F. 2018, ApJ, 867, 20
Cheng, Z., Méndez, M., Altamirano, D., Beri, A., & Wang, Y. 2019, MNRAS, 482, 550
Coughlin, E. R., & Nixon, C. J. 2019, ApJL, 883, L17
Dewangan, G. C., Titarchuk, L., & Griffiths, R. E. 2006, ApJL, 637, L21
Drout, M. R., Chornock, R., Soderberg, A. M., et al. 2014, ApJ, 794, 23
Farrell, S. A., Webb, N. A., Barret, D., Godet, O., & Rodrigues, J. M. 2009, Natur, 460, 73
Golightly, E. C. A., Nixon, C. J., & Coughlin, E. R. 2019, ApJL, 882, L26
Greene, J. E., Strader, J., & Ho, L. C. 2020, ARA&A, 58, 257
Guillochon, J., & Ramirez-Ruiz, E. 2013, ApJ, 767, 25
Ho, A. Y. Q., Perley, D. A., Gal-Yam, A., et al. 2021, arXiv:2105.08811
Ho, A. Y. Q., Phinney, E. S., Ravi, V., et al. 2019, ApJ, 871, 73
Huang, K., Shimoda, J., Urata, Y., et al. 2019, ApJ, 878, L25
Ingram, A. R., & Motta, S. E. 2019, NewAR, 85, 101524
Kuin, N. P. M., Wu, K., Oates, S., et al. 2019, MNRAS, 487, 2505
Kumar, P., Narayan, R., & Johnson, J. L. 2008, MNRAS, 388, 1729
Leahy, D. A., Darbro, W., Elsner, R. F., et al. 1983, ApJ, 266, 160
Lin, D., Guillochon, J., Komossa, S., et al. 2017, NatAs, 1, 0033
Lin, D., Strader, J., Carrasco, E. R., et al. 2018, NatAs, 2, 656
Lyman, J. D., Galbany, L., Sánchez, S. F., et al. 2020, MNRAS, 495, 992
Margutti, R., Metzger, B. D., Chornock, R., et al. 2019, ApJ, 872, 18
Mockler, B., Guillochon, J., & Ramirez-Ruiz, E. 2019, ApJ, 872, 151
Mohan, P., An, T., & Yang, J. 2020, ApJL, 888, L24
Morgan, E. H., Remillard, R. A., & Greiner, J. 1997, ApJ, 482, 993
Morokuma-Matsui, K., Morokuma, T., Tominaga, N., et al. 2019, ApJL, 879, L13
Noyola, E., Gebhardt, K., & Bergmann, M. 2008, ApJ, 676, 1008
Pasham, D. R., Cenko, S. B., Zoghbi, A., et al. 2015, ApJL, 811, L11
Pasham, D. R., Ho, W. C. G., Alston, W., et al. 2021, NatAs, 6, 249
Pasham, D. R., Remillard, R. A., Fragile, P. C., et al. 2019, Sci, 363, 531
Perley, D. A., Mazzali, P. A., Yan, L., et al. 2019, MNRAS, 484, 1031
Piran, T., Svirski, G., Krolik, J., Cheng, R. M., & Shiokawa, H. 2015, ApJ, 806, 164
Prentice, S. J., Maguire, K., Smartt, S. J., et al. 2018, ApJL, 865, L3
Pursiainen, M., Childress, M., Smith, M., et al. 2018, MNRAS, 481, 894
Ramirez-Ruiz, E., & Rosswog, S. 2009, ApJL, 697, L77
Rees, M. J. 1988, Natur, 333, 523
Reis, R. C., Miller, J. M., Reynolds, M. T., et al. 2012, Sci, 337, 949
Remillard, R. A., & McClintock, J. E. 2006, ARA&A, 44, 49
Revnivtsev, M., Churazov, E., Gilfanov, M., & Sunyaev, R. 2001, A&A, 372, 138
Rivera Sandoval, L. E., Maccarone, T. J., Corsi, A., et al. 2018, MNRAS, 480, L146
Roychowdhury, S., Arabsalmani, M., & Kanekar, N. 2019, MNRAS, 485, L93
Shaposhnikov, N., & Titarchuk, L. 2009, ApJ, 699, 453
Song, J. R., Shu, X. W., Sun, L. M., et al. 2020, A&A, 644, L9
Strohmayer, T. E., & Mushotzky, R. F. 2009, ApJ, 703, 1386
Sun, N.-C., Maund, J. R., Crowther, P. A., & Liu, L.-D. 2022, MNRAS, 512, L66
Timmer, J., & Koenig, M. 1995, A&A, 300, 707
Tse, K., Galloway, D. K., Chou, Y., Heger, A., & Hsieh, H.-E. 2021, MNRAS, 500, 34
Uttley, P., McHardy, I. M., & Papadakis, I. E. 2002, MNRAS, 332, 231
Vaughan, S. 2010, MNRAS, 402, 307
Vignarca, F., Migliari, S., Belloni, T., Psaltis, D., & van der Klis, M. 2003, A&A, 397, 729
Zhou, X.-L., Yuan, W., Pan, H.-W., & Liu, Z. 2015, ApJL, 798, L5